crystals

MDPI

Article

Enhanced Strength–Ductility Synergy of Mg-Al-Sn-Ca Alloy via Composite Asymmetric Extrusion

Xiwen Chen [1], Yuxuan Li [2], Zhigang Li [2,*], Chao Wang [3] and Hai Deng [3,*]

[1] Vehicle Department, Guangzhou Railway Bureau Group Company, Guangzhou 510100, China; mapleleaf2000@163.com
[2] Key Laboratory of Automotive Materials Ministry of Education & School of Material Science and Technology, Jilin University, Changchun 130022, China; yuxuanl21@mails.jlu.edu.cn
[3] National Railway Vehicle Engineering Research Center, CRRC Changchun Railway Vehicles Co., Ltd., Changchun 130062, China; wangchao5.ck@crrcgc.cc
* Correspondence: lzg@jlu.edu.cn (Z.L.); denghai.ck@crrcgc.cc (H.D.)

Abstract: Fine-grain and weak-texture magnesium alloys are the long-term development targets of lightweight structural materials. In this study, a new composite asymmetric extrusion (CAE) is developed, which, coupling with an asymmetric die and an asymmetric billet, is proposed to improve the strength–ductility of the Mg-3.8Al-1.1Sn-0.4Ca alloy. The influence of the asymmetric billet on the microstructure and mechanical properties was investigated. The findings revealed that the asymmetric billet can induce greater plastic deformation, resulting in an increase in the cumulative strain and an improved nucleation rate. The CAE sheets exhibit fine grains (4.4 μm) and a weak tilted texture (7.57 mrd). Furthermore, the asymmetric billet results in the microstructure not forming a gradient microstructure under gradient strain along the transverse direction (TD) direction. The CAE sheets exhibited good mechanical properties, with a yield strength (YS) of 253 MPa, ultimate tensile strength (UTS) of 331 MPa, and elongation (EL) of 20%. This development shows promise in achieving high-efficiency, low-cost production of magnesium alloys.

Keywords: Mg alloy; composite asymmetric extrusion; microstructure; texture

Citation: Chen, X.; Li, Y.; Li, Z.; Wang, C.; Deng, H. Enhanced Strength–Ductility Synergy of Mg-Al-Sn-Ca Alloy via Composite Asymmetric Extrusion. *Crystals* **2024**, *14*, 323. https://doi.org/10.3390/cryst14040323

Academic Editors: Erdem Karakulak and Huseyin Sevik

Received: 3 March 2024
Revised: 27 March 2024
Accepted: 29 March 2024
Published: 30 March 2024

1. Introduction

In the background of energy conservation and emission reduction, the utilization of lightweight structural materials represents an effective strategy [1]. Given its low density, high specific strength, and exceptional electromagnetic shielding properties [2], the advancement of magnesium structural materials remains a prominent research focus [3]. Nonetheless, the constrained ductility and strength of magnesium alloys [4] limit their wide industrial application. Additionally, extrusion speed is also a critical factor limiting the industrial application of magnesium alloy extrusion forming. An increase in the extrusion rate typically leads to larger grain sizes and surface defects, significantly impacting the quality of the extruded products. High-speed extrusion, while offering substantial advantages in enhancing industrial productivity and reducing costs, also raises the squeezing pressure. A tenfold increase in extrusion speed can result in a 50% elevation in extrusion pressure, necessitating the use of magnesium alloys that are capable of withstanding high temperatures. Particularly, the rapid deformation rate during high-speed extrusion causes a more significant increase in temperature compared to low-speed extrusion, exacerbating the risk of thermal cracking issues. Furthermore, the substantial heat generated during high-speed extrusion often results in a coarse grain structure, ultimately reducing the strength. Hence, the key to meeting the practical industrial application of magnesium alloys lies in achieving strength and ductility cooperation among magnesium alloys under high-speed extrusion conditions.

Adding alloying elements and modifying the deformation mechanism represent effective strategies for enhancing the strength and ductility of magnesium alloys [5]. Among these, Mg-Al-based alloys stand out as the most commonly utilized alloy system due to their favorable combination of strength and ductility [6,7]. The Sn element can decrease the layer fault energy and form Mg2Sn with a high-temperature melting point phase, which can impede the growth of dynamic recrystallized grains and enhance the strength and ductility of Mg-Al alloys [8]. For example, Sasaki et al. [9] demonstrated the fabrication of an Mg-Sn-Zn-Al alloy through low-temperature extrusion, resulting in a fine grain structure with a high yield strength (YS) of 347 MPa. Additionally, the incorporation of Ca has been extensively studied, as its addition effectively improves strength and ductility owing to its similar atomic size to rare earths [10]. Pan et al. [11] achieved an exceptional combination of YS (425 MPa) and elongation (EL) (11%) for the Mg-1.0Ca-1.0Al-0.2Zn-0.1Mn alloy. Furthermore, Ca in Mg-Al-Sn-based alloys contributes to the formation of the hard reinforcement phase CaMgSn. Zha et al. [12] conducted controlled rolling of an Mg-4.5Al-1.5Sn-0.5Ca alloy, resulting in outstanding mechanical properties with a YS of 275 MPa and an EL of 20%, attributed to the formation of nano-sized CaMgSn precipitates (~16 nm). Consequently, Mg-Al-Sn-Ca alloys hold significant promise for the development of high-strength and high-ductility materials.

The deformation process of Mg alloys primarily involves dislocation slip and twinning deformation. Grain boundaries, functioning as regions of atomic disorder, hinder the movement of dislocations/twins, thereby enhancing the yield strength of the magnesium alloy. Compared to face center cubic (FCC) and body center cubic (BCC) structures, the hexagonal close packing (HCP) structure of magnesium alloys manifests a more significant grain boundary strengthening effect. Consequently, grain refinement emerges as a pivotal factor in bolstering the strength of the magnesium alloy. Severe plastic deformation (SPD) processes are effective strategies to refine grain size [13], such as equal access angle extrusion (EASE) [14] and cyclic extrusion (CEC) [15]. However, it is difficult to obtain ultra-fine-grain magnesium alloys via single-pass hot extrusion and it is easy to have a strong basal texture, resulting in poor formability of magnesium alloys [16]. SPD processes are complex and costly, and the forming efficiency and sample size are much lower than extrusion, limiting its application. Recent advancements have seen a shift towards unconventional processing routes, such as asymmetric extrusion, as a means to address the limitations of conventional methods. Researchers have discovered that the microstructure and mechanical properties of magnesium alloys can be substantially modified by altering the extrusion die structure and billet [17]. Wang et al. [18] obtained a uniform fine-grain microstructure with inclined texture via differential speed extrusion. The AZ31 sheets exhibit a high ultimate tensile strength (352.8 MPa). The design of a special die structure can enhance the degree of shear deformation during extrusion. Nevertheless, it is challenging to flexibly improve the die structure in response to changing actual requirements. Additionally, the design and fabrication of the mold structure are notably more intricate compared to traditional extrusion processes. Consequently, researchers have undertaken numerous endeavors to explore alternative approaches, focusing on the structure and loading methodology of the billet. He et al. [19] divided AZ31 ingots into several pieces, thereby influencing the effective strain evolution through the introduction of a specific interface during extrusion. This approach resulted in a high strength, with a YS of 303 MPa. However, the mechanical properties of sheets produced using certain existing asymmetric extrusion processes vary in the direction of the strain gradient, ultimately leading to a reduction in overall mechanical properties.

In the present study, the Mg-3.8Al-1.1Sn-0.4Ca alloy was prepared using composite asymmetric extrusion (CAE), offering an efficient approach to enhance both the strength and ductility. By altering the shape of the billet, not only can we refine grains effectively, but the texture can also be weakened, leading to an enhancement in the mechanical properties. We have uncovered the underlying mechanisms responsible for the enhancement of strength and ductility. Moreover, the composite asymmetric extrusion method employed in this

research obviates the need for a repetitive deformation procedure, indicating a simple and effective approach for enhancing mechanical properties, which is a requisite in the SPD process.

2. Materials and Methods

The Mg-3.8Al-1.1Sn-0.4Ca alloy used in this experiment was cast with Mg, Al, and Sn metal ingots and Mg-20Ca (wt.%) master alloy. First, the pure Mg was placed into the resistance furnace, and the temperature is raised to 680 °C for 1 h. Then, the Al, Sn, and Mg-20Ca (wt.%) alloys were placed into the resistance furnace. Once the added alloys had fully melted, we proceeded with the following steps sequentially: stirring (utilizing a tool to stir the melt up and down to ensure even mixing of the alloys), blowing (introducing argon into the melt to eliminate impurities), and slagging (using a slagging spoon to remove impurities from the surface of the melt). Finally, after restoring the melt temperature to 680 °C, we poured the resulting melt into the copper mold. Subsequently, the as-cast alloy underwent a multi-stage homogenization treatment (375 °C/3 h + 430 °C/2 h + 480 °C/3 h), followed by water quenching to retain the high-temperature organization. The extruded sample was cut on the as-homogenized alloy. The shape and size of the billet are shown in Table 1. In addition, the extrusion die used in this experiment was an asymmetric extrusion die, and the ratio of the length on the left side of the extrusion exit channel to the length on the right side was 1.5 [20]. Before extrusion, the billets underwent preheating at 400 °C for 1 h, while the die was preheated to the same temperature of 400 °C. After extrusion, they were cooled in water immediately. The sheets extruded via asymmetric extrusion and composite asymmetric extrusion were designated as AE and CAE, respectively. A schematic diagram illustrating the sheet-forming process is depicted in Figure 1. The extrusion ratio was 21:1, with a ram speed of 16 mm/s.

Table 1. Billet shape and size for AE and CAE processes.

Sample	Billet Shape	Size
AE	square-shaped	70 mm × 45 mm × 10 mm
CAE	trapezoid-shaped	10 mm (top), 70 mm (bottom), 45 mm (height), and 10 mm (thickness)

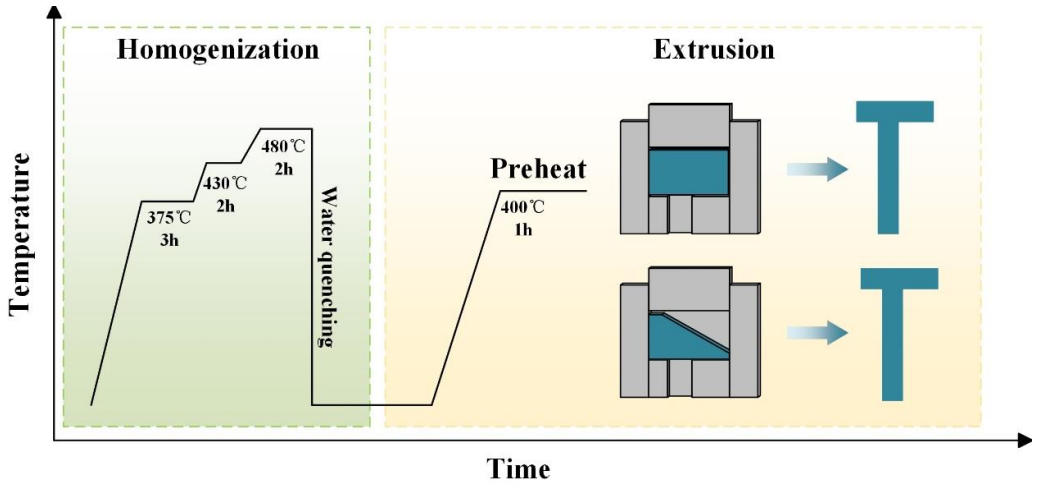

Figure 1. Schematic illustration of the preparation process of AE sheets and CAE sheets.

A microstructural characterization was performed using a scanning electron microscope (SEM, ZEISS, Sigma 500, Chiyoda, Japan) and electron backscattered diffraction (EBSD, Oxford Symmetry, London, United Kingdom). SEM and EBSD samples were ground using SiC papers of different grit sizes (#600 to #7000), followed by mechanical polishing. The EBSD samples were electro-polished using an AC_2 solution for 60–120 s.

The area fraction and size of the second phases were analyzed using Image-Pro Plus 6.0 software, and each sample was measured three times.

Transmission electron microscopy (TEM) analysis was performed using the FEI Talos F200X instrument. The sample preparation process for TEM involved several steps: manual grinding, electrolytic double spray, and ion thinning. Firstly, the sample was ground using SiC sandpaper to approximately 80 μm in thickness and then punched into a 3 mm diameter round sheet. Then, electrolytic double spraying of the disc was carried out using the RL-2 intelligent thinning instrument at −45 °C and 30 V. The electrolyte solution comprised 860 mL of ethanol and 40 mL of perchloric acid, and the process was halted immediately upon the appearance of a hole in the center of the disc. Finally, ion thinning was performed, with the sample temperature controlled using liquid nitrogen to approximately −150 °C to prevent thermal effects.

Finite element simulation analysis for the extrusion process in this study involved the use of DEFORM-3D 11.0 software. The friction coefficient was set to 0.25. The temperature was specified as 400 °C, with an extrusion speed set at 16 mm/s.

Tensile samples were machined into a dog-bone shape with dimensions of 30 mm × 10 mm × 1 mm from both the AE sheets and CAE sheets, oriented along the extrusion direction (ED). The gauge length of the tensile samples was 10 mm. Before conducting the tensile test, the surface of each sample was meticulously polished with sandpaper to eliminate any oxide film and surface defects. This preparatory step was crucial for enhancing the accuracy of the obtained mechanical properties. Tensile tests were conducted using an INSTRON 1121 universal testing machine, which was coupled with a video extensometer at a strain rate of 1.0×10^{-3} s^{-1}. To ensure the repeatability of mechanical properties, at least three samples from each extruded sheet were tested.

3. Results

3.1. Mechanical Properties

Figure 2a showcases the room-temperature tensile stress–strain curves of the AE and CAE sheets, and Figure 2b provides a comparative analysis of their mechanical properties. It is evident from the comparison that the mechanical properties of the CAE sheets surpassed those of the AE sheets. Specifically, the average yield strength (YS) and ultimate tensile strength (UTS) were recorded as 253 ± 4 MPa and 331 ± 3 MPa, respectively. In contrast, the CAE sheets demonstrated a notable increase in both YS and UTS of 33 MPa and 12 MPa, respectively, compared to the AE sheets. Additionally, the average elongation (EL) rose from 17 ± 1% to 20 ± 2%. These results signify that the CAE sheets exhibited a commendable strength and ductility balance.

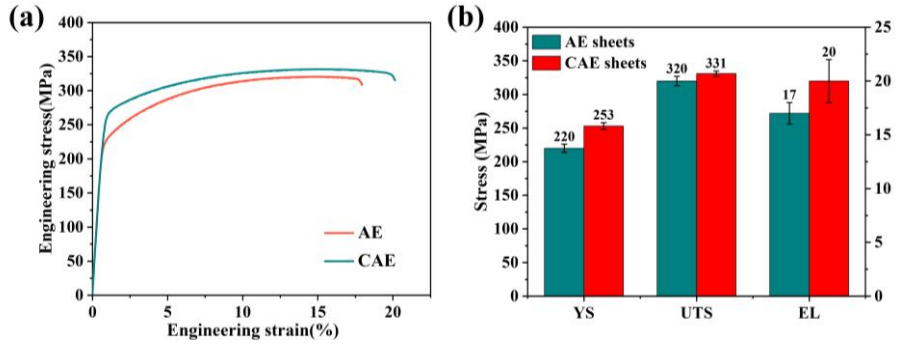

Figure 2. (**a**) Room-temperature tensile curves; (**b**) comparison of mechanical properties of AE sheets and CAE sheets.

3.2. Microstructures and Textures

Figure 3a,d displays the inverse pole figures (IPFs) of the AE sheets and CAE sheets. The AE sheets exhibited a characteristic bimodal structure, which consisted of coarse undynamic recrystallized (unDRXed) grains and fine dynamic recrystallized (DRXed)

grains. The average grain size was 7.4 ± 4.8 μm. After the CAE process, the average grain size decreased to 4.4 ± 2.1 μm. The microstructure was typified by the presence of fine DRXed grains with a similar size. These findings suggest that the CAE process can refine the grain size and yield a uniform microstructure.

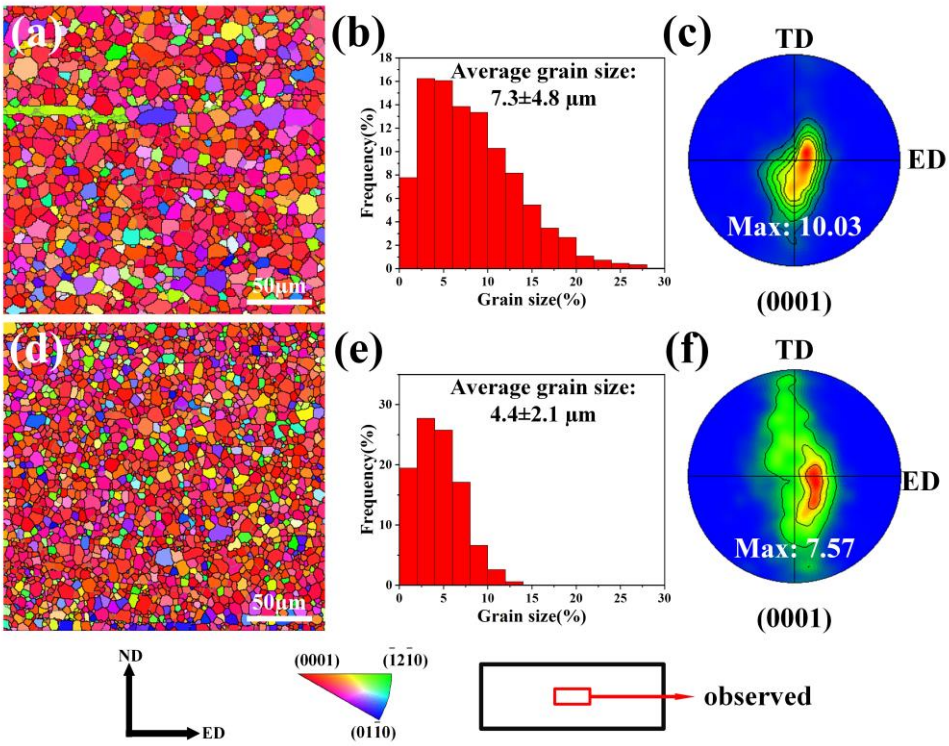

Figure 3. Inverse pole figure (IPF) maps, grain size distributions, and (0002) PFs of: (**a**–**c**) AE sheets and (**d**–**f**) CAE sheets.

Figure 3c,f depicts the pole figures (PFs) of AE sheets and CAE sheets. Both exhibited a typical asymmetric extrusion texture, in which the c-axis of the majority the grains deviated from the normal direction (ND) to the extrusion direction (ED) [21]. In this study, the maximum density of the AE sheets and the CAE sheets was titled about 20°–30° from ND to ED. After the CAE process, a distinct evolution in texture was observed, with the maximum intensity decreasing to 7.57 mrd. This decline suggests a weakening of the texture in the CAE sheet.

Figure 4 shows the SEM images and the corresponding EDS results of the AE sheets and the CAE sheets. The EDS results revealed that the predominant second phase in both the AE sheets and the CAE sheets was the CaMgSn phase, with a minor presence of the $(Mg, Al)_2Ca$ phase. After the AE and CAE processes, the coarse CaMgSn phases underwent fragmentation and exhibited a characteristic extrusion streamline. According to the statistics, the area fraction of the CaMgSn phase in the AE sheets and the CAE sheets were 1.584%, and 1.123%, respectively. In the enlarged images, it becomes apparent that the CaMgSn phase in the AE sheets experienced inadequate fragmentation, featuring cracks. Conversely, the CaMgSn phases of the CAE sheets underwent thorough fragmentation, resulting in finer CaMgSn phases. Furthermore, compared with the concentrated distribution in the AE sheets, the distribution of the CaMgSn phases in the CAE sheets appears more dispersed. This might be related to the greater plastic deformation introduced by the CAE process.

The reduction in the area fraction of the micron-sized CaMgSn phase observed in the CAE sheets (Figure 4) suggests the potential formation of more nano-sized CaMgSn phases in these sheets. It is inferred that the refinement and random distribution of the CaMgSn phases contribute to the higher YS. Figure 5 presents the brightfield TEM images of both the AE sheets and the CAE sheets, revealing that the nano-sized CaMgSn phases existed

in both materials. Compared with the AE sheets, the CaMgSn phases in the CAE sheets exhibited a decreased size, and the morphology transformed from irregular block shapes to short rod shapes. Moreover, the nano-sized CaMgSn phase density in the CAE sheets was higher, and the distribution appeared to be more random compared to the AE sheets.

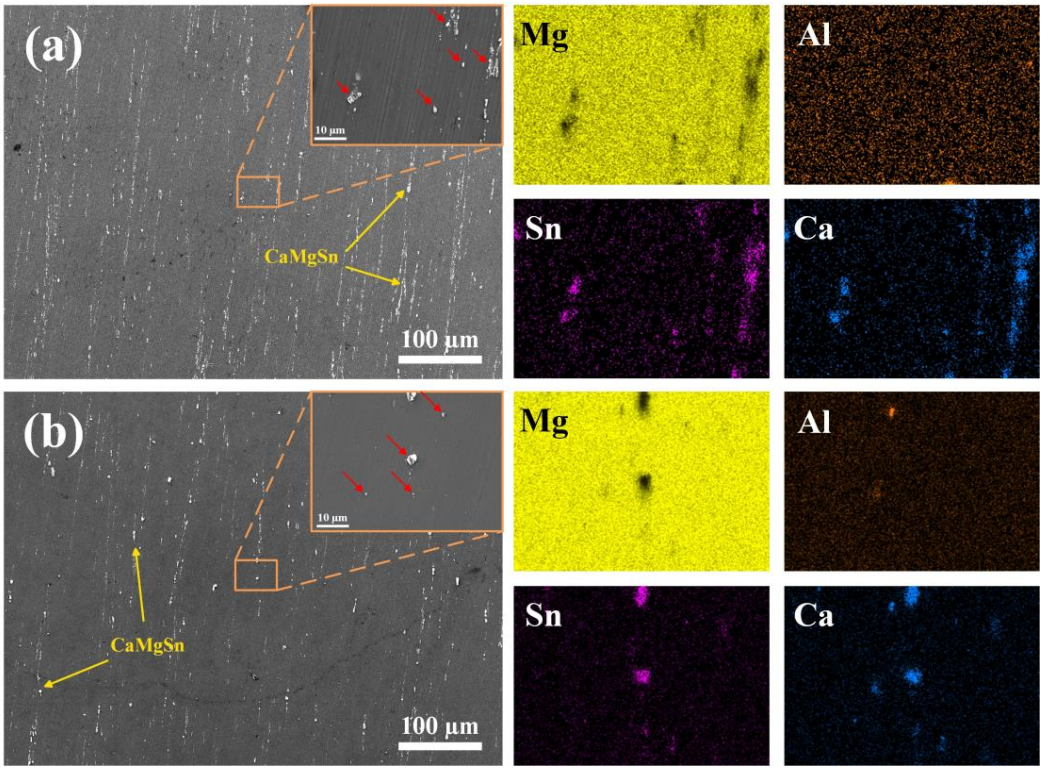

Figure 4. SEM images and the corresponding EDS results: (**a**) AE sheets (**b**) CAE sheets.

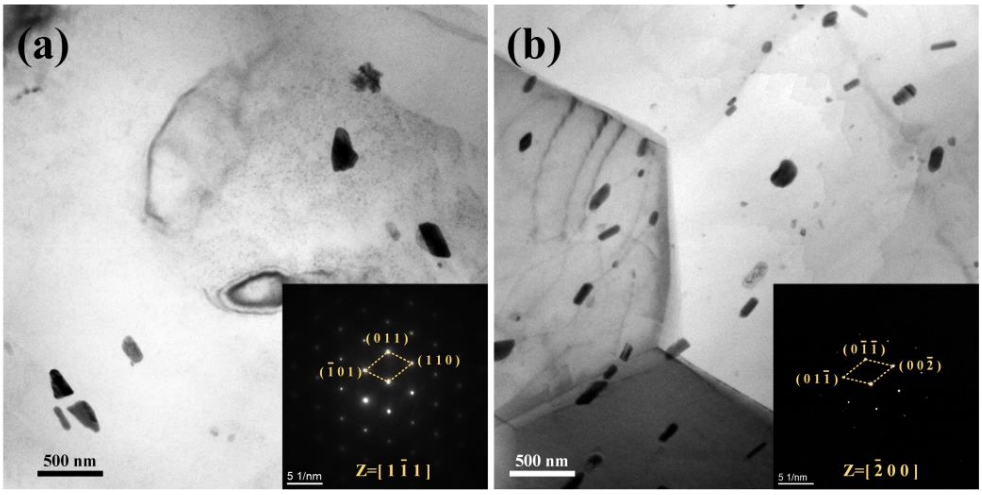

Figure 5. The bright-field TEM images: (**a**) AE sheets, (**b**) CAE sheets.

4. Discussion

4.1. Microstructure Analysis

The CAE sheets demonstrated a uniformly fine grain structure and a weak tilted texture in comparison to the AE sheets. To explore the impact of the asymmetric billet in the extrusion process, the microstructure evolution near the die outlet in both the AE and CAE processes was studied, as shown in Figure 6. In the case of the AE process, the microstructure near the die outlet comprised coarse grains with interspersed fine grains.

Conversely, the CAE sheets exhibited a distinct microstructure, with grains notably refined at the corresponding position. Additionally, an increased area fraction of DRXed grains was observed. This divergence suggests that the asymmetric billet induces greater plastic deformation, consequently amplifying the cumulative strain experienced by the parent grains and thereby enhancing the nucleation rate [22,23].

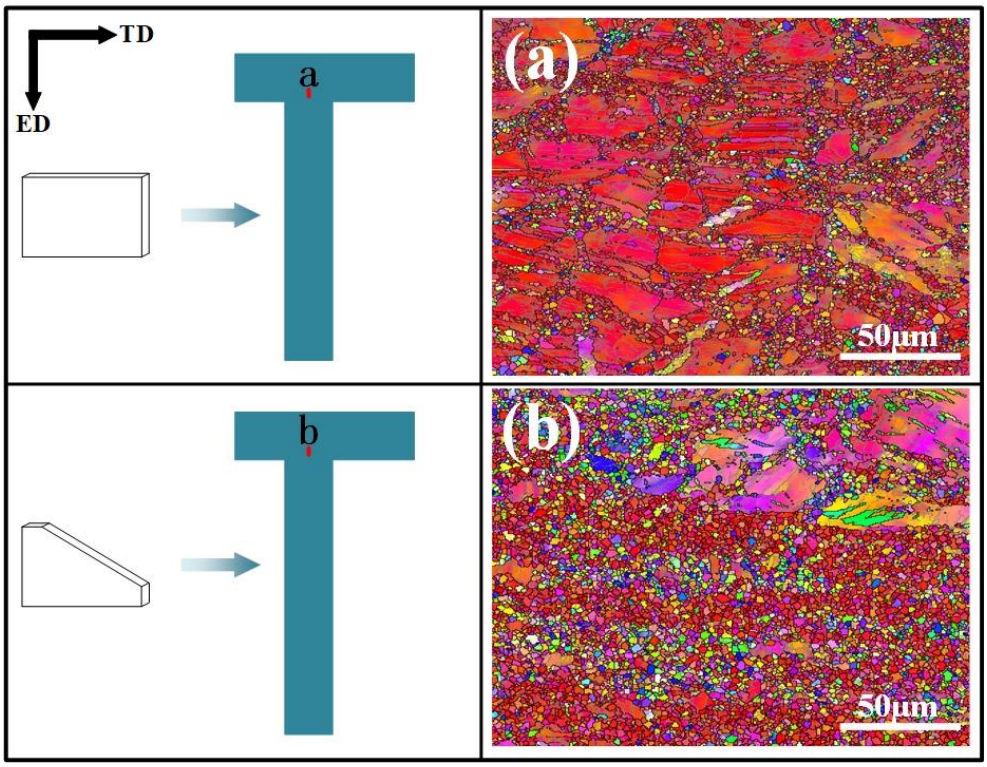

Figure 6. Microstructure near the die outlet: (**a**) AE sheets, (**b**) CAE sheets.

Figure 7 depicts the simulated distribution of effective stress and strain during the extrusion process of AE and CAE. Notably, it was observed that the effective stress and strain at the extrusion outlet exhibited asymmetrical distribution for both billets. Along the transverse direction (TD), there existed a gradient distribution of effective stress and strain. Compared to the square billets, the asymmetric billets underwent pre-extrusion influences from other parts, leading to a continuous accumulation of strain. Consequently, significant shear deformation was experienced at the exit of the die orifice, further increasing the equivalent strain of the extruded sheet.

In the CAE process, the formation of a gradient microstructure is attributed to the gradient strain, which influences both the microstructure uniformity and mechanical properties [24]. In order to explore the microstructure uniformity of CAE sheets in the strain gradient direction, the microstructure along the transverse direction (TD) of the CAE sheets was studied. The microstructure at the left, middle, and right position along the TD direction of the CAE sheets are shown in Figure 8. Remarkably, the microstructure of the three positions appears consistent, with grain sizes measuring 4.3 μm, 4.4 μm, and 4.6 μm from left to right, respectively. Additionally, the texture has an evolution along gradient distribution, with the maximum texture intensity decreasing from 10.26 mrd to 5.49 mrd. The asymmetric billet enhances the cumulative strain by increasing the plastic deformation at the low strain position, resulting in minimal microstructural differences across the gradient strain in the CAE sheets.

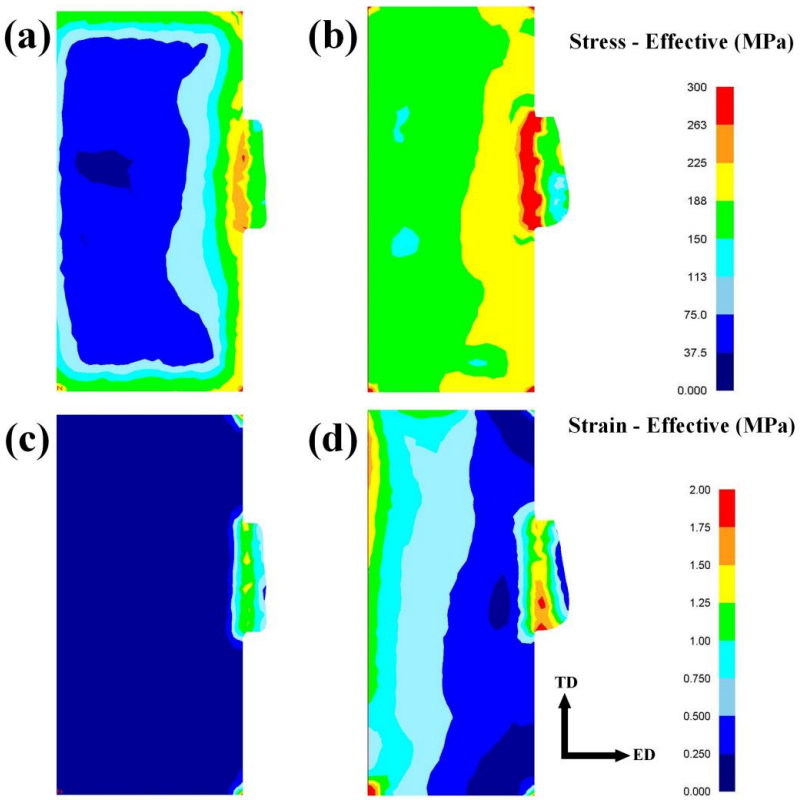

Figure 7. Effective stress and effective strain distributions in (**a**,**c**) AE and (**b**,**d**) CAE processes.

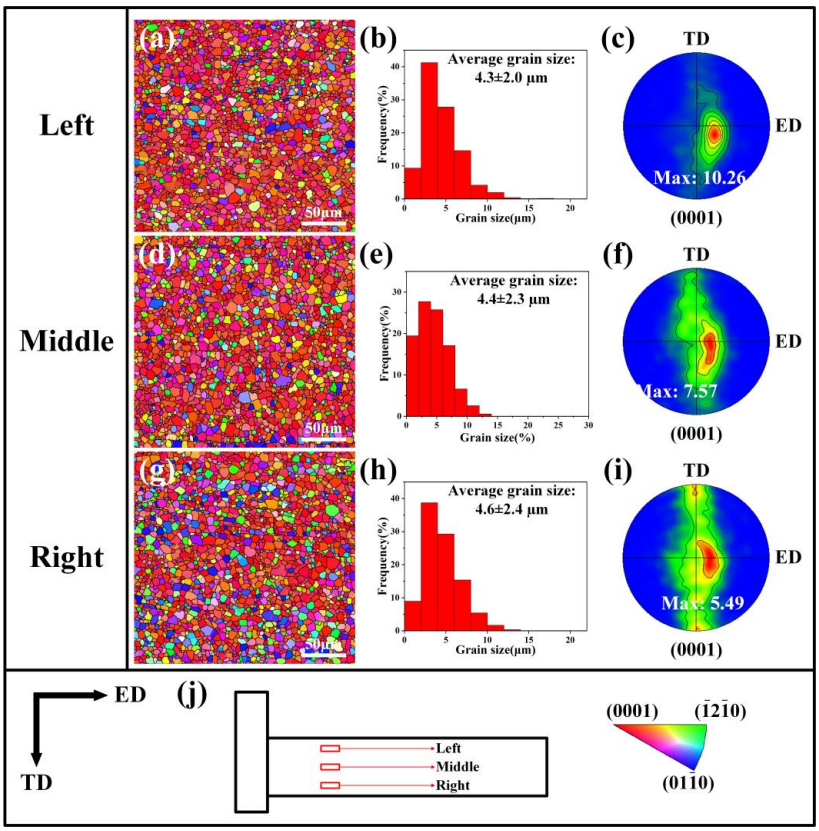

Figure 8. Microstructures of the (**a**–**c**) left position, (**d**–**f**) middle position, and (**g**–**i**) right position along the TD direction with corresponding (0002) pole figures of CAE sheets; (**j**) sampling position.

4.2. Analysis of Mechanical Properties

In comparison to the AE sheets, the CAE sheets exhibited a higher yield strength. The YS of the CAE sheet was 253 ± 4 MPa. The asymmetric billet underwent greater shear deformation, resulting in increased accumulated strain during extrusion. This promotes DRXed grain nucleation. The microstructure analysis suggests that the increased YS of the CAE sheets primarily resulted from fine grain strengthening. The grain boundary strengthening contribution can be quantified using the Hall–Petch formula [25]:

$$\sigma_{GB} = \sigma_0 + kd^{-1/2} \quad (1)$$

where σ_0 represents the friction stress, k signifies the Hall–Petch coefficient [26], and d represents the average grain size. The average grain sizes of the AE sheets and the CAE sheets in this study were recorded as 7.3 μm and 4.4 μm. Thus, the contribution of grain boundary strengthening for the AE sheets and the CAE sheets was 166.9 MPa and 189.1 MPa, respectively.

Additionally, considering that the CaMgSn phases exhibited different sizes and distributions in the AE sheets and the CAE sheets and are known to be hard-reinforced phases, precipitation strengthening can be calculated via Orowan strengthening [27]:

$$\sigma_{Orowan} = M\frac{Gb}{2\pi\sqrt{1-\nu}\left(\frac{0.953}{\sqrt{f}}-1\right)d_p}\ln\frac{d_p}{b}\ldots \quad (2)$$

where M represent the Taylor factor (~2.5), G is shear modulus (~1.7 GPa), ν is Poisson's ratio (~0.3), and b signifies the Burgers vector (0.32 nm). In addition, dp and f represent the diameter and volume fraction of the CaMgSn phases in this study, respectively [28]. The values of d_p and f in the AE sheets and the CAE sheets are listed in Table 2. The calculated d_p and f values for the CAE sheet and the AE sheet alloys were approximately 25.6 MPa and 42.6 MPa, respectively. Simultaneously, second-phase particles play a crucial role in recrystallization. The small size of the CaMgSn phases can typically hinder grain boundary movement and decelerate DRXed grain growth via the Zener drag effect. Meanwhile, CaMgSn particles can expedite recrystallization through particle-stimulated nucleation (PSN) owing to the significant energy stored in the CAE deformation region. Furthermore, the solute drag effect complicates the grain boundaries' mobility. Zener pinning of fine particles and solute dragging of alloying elements in solution both impede the migration of grain boundaries, albeit through different mechanisms.

Table 2. Values of d_p and f in AE sheets and CAE sheets.

Value	AE	CAE
	Nano-sized precipitates CaMgSn	Nano-sized precipitates CaMgSn
d_p (nm)	440	180
f (%)	0.13	0.28

The calculated combined effects of grain boundary strengthening and precipitation strengthening contributing to the YS of AE sheets and CAE sheets are estimated at 192.5 MPa and 231.7 MPa, respectively. However, there seems to be a discrepancy between the calculated value and the measured value. This difference could potentially be attributed to the contribution of solute segregation.

Figure 9 illustrates the kernel average misorientation (KAM) of the AE sheets and the CAE sheets. It is evident that residual strain persists in the deformed grains of the AE sheets, with lower residual strain observed in the recrystallized grains. In contrast, the CAE sheets exhibit almost no residual strain compared to the AE sheets, indicating a very low geometrically necessary dislocation density in the CAE sheets. Consequently,

the dislocation strengthening contribution in the AE sheets and the CAE sheets is deemed insignificant. Thus, the effect of dislocation strengthening on the YS is disregarded in this study.

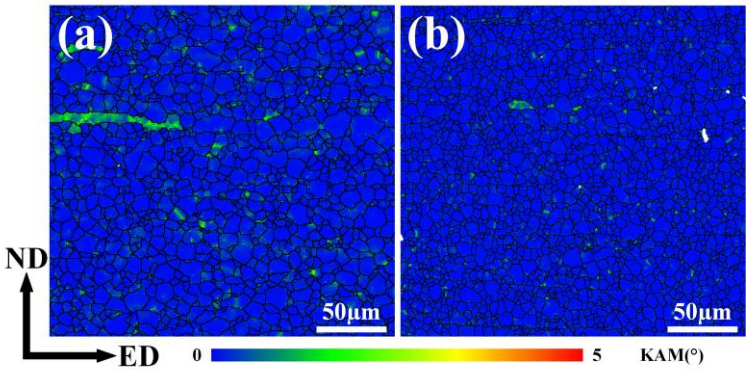

Figure 9. KAM maps of: (**a**) AE sheets, (**b**) CAE300 sheets.

Figure 10 presents Schmid factor (SF) maps along with the SF distribution in the AE sheets and the CAE sheets. Generally, the SF value signifies the propensity for activation of a specific slip mode relative to the loading direction, with higher SF values indicating easier activation of slip. Notably, the SF of the basal <a> slip in the CAE sheets was observed to be smaller compared to the AE sheets, with an average SF value of 0.31 $\pm$ 0.3. The lower SF value implies that the activation of slip was more difficult in the CAE sheets, thereby suggesting a higher YS.

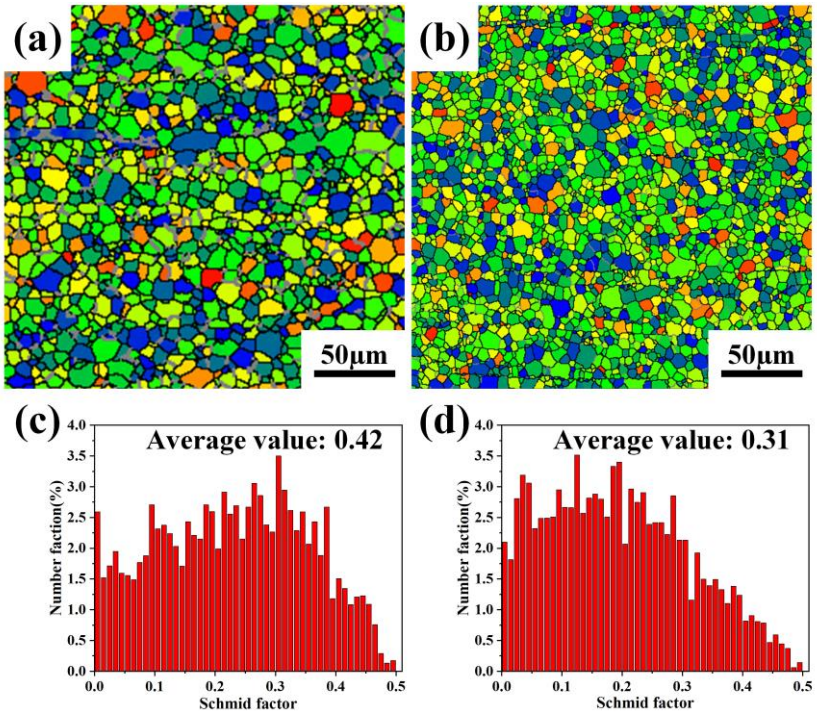

Figure 10. Basal SF distributions of <a> slip and histogram of average Schmid factor distribution. (**a**,**b**) AE sheets, (**c**,**d**) CAE sheets.

In general, magnesium alloys exhibiting higher strengths often experience a reduction in ductility. Nevertheless, the CAE sheets in this study demonstrated good ductility. This favorable ductility primarily stemmed from the uniformly fine DRXed grain structure. The fine grain structure facilitated coordinated deformation of grain boundaries and enhanced the cooperative ability of grain boundaries during deformation [29]. Furthermore, the CAE

sheets exhibited a weak tilted texture, indicating that a large number of grains are conducive to orientation deformation. Consequently, the CAE sheets achieved a commendable strength and ductility balance.

5. Conclusions

In this study, the effects of AE and CAE processes on microstructure and mechanical properties were thoroughly analyzed, with a specific focus on microstructure evolution during the CAE process. The conclusions are as follows:

1. The utilization of an asymmetric billet in the CAE process induces greater plastic deformation compared to the AE process. This increased plastic deformation enhances the cumulative strain and promotes nucleation, resulting in a higher nucleation rate in CAE sheets.
2. The CAE sheets exhibited a weakened texture compared to the AE sheets, and the maximum texture intensity was 7.57 mrd. This suggests that the CAE process alters the texture evolution during extrusion.
3. The mechanical properties of the CAE sheets exhibited simultaneous improvements in strength and ductility. These sheets demonstrated excellent mechanical characteristics (YS: 253 $\pm$ 4 MPa and EL: 20 $\pm$ 2%). The elevated YS was primarily ascribed to the reinforcement mechanisms of grain boundary strengthening and precipitation strengthening. Meanwhile, the good ductility owes largely to the uniform microstructure, weak tilted texture, and random distribution of the nanoscale CaMgSn phases.

Author Contributions: Conceptualization, Z.L. and H.D.; methodology, Y.L. and Z.L.; formal analysis, C.W.; investigation, C.W.; data curation, X.C. and H.D.; writing—original draft preparation, Y.L.; writing—review and editing, Y.L. and X.C; supervision, Z.L.; funding acquisition, Z.L. All authors have read and agreed to the published version of the manuscript.

Funding: Financial support from the National Natural Science Foundation of China (52271031) and the National Key Research and Development Program (No. 2022YFB4301201, 2022YFB4301202), as well as partial financial support from the Science and Technology Development Program of Jilin Province (20240301033GX) are gratefully acknowledged.

Data Availability Statement: The original contributions presented in the study are included in the article, further inquiries can be directed to the corresponding authors.

Acknowledgments: The authors declare that they have no known competing financial interests or personal relationships that could have appeared to influence the work reported in this paper.

Conflicts of Interest: Xiwen Chen is employed by the company Guangzhou Railway Bureau Group Company, and Chao Wang, and Hai Deng are employed by the company CRRC Changchun Railway. The remaining authors declare that the research was conducted in the absence of any commercial or financial relationships that could be construed as a potential conflict of interest.

References

1. Yang, Y.; Xiong, X.; Chen, J.; Peng, X.; Chen, D.; Pan, F. Research advances of magnesium and magnesium alloys worldwide in 2022. *J. Magnes. Alloys* **2023**, *11*, 2611–2654. [CrossRef]
2. Song, J.; Chen, J.; Xiong, X.; Peng, X.; Chen, D.; Pan, F. Research advances of magnesium and magnesium alloys worldwide in 2021. *J. Magnes. Alloys* **2022**, *10*, 863–898. [CrossRef]
3. Gao, M.; Etim, I.P.; Yang, K.; Tan, L.; Ma, Z. Enhancing mechanical property and corrosion resistance of Mg–Zn-Nd alloy wire by a combination of SPD techniques, extrusion and hot drawing. *Mater. Sci. Eng. A* **2022**, *829*, 142058. [CrossRef]
4. Cheng, Y.Q.; Chen, Z.H.; Xia, W.J.; Zhou, T. Improvement of Drawability at Room Temperature in AZ31 Magnesium Alloy Sheets Processed by Equal Channel Angular Rolling. *J. Mater. Eng. Perform.* **2008**, *17*, 15–19. [CrossRef]
5. Li, Z.-G.; Miao, Y.; Jia, H.-L.; Zheng, R.; Wang, M.-H.; Wang, H.-Y. Designing a low-alloyed Mg–Al–Sn–Ca alloy with high strength and extraordinary formability by regulating fine grains and unique texture. *Mater. Sci. Eng. A* **2022**, *852*, 143687. [CrossRef]
6. Nakata, T.; Xu, C.; Matsumoto, Y.; Shimizu, K.; Sasaki, T.T.; Hono, K.; Kamado, S. Optimization of Mn content for high strengths in high-speed extruded Mg-0.3Al-0.3Ca (wt%) dilute alloy. *Mater. Sci. Eng. A* **2016**, *673*, 443–449. [CrossRef]
7. Li, M.-Y.; Guan, Z.-P.; Liu, L.-P.; Jia, H.-J.; Li, Z.-G.; Wang, M.-H.; Ma, P.-K.; Song, J.-W. Investigation of enhanced strength anisotropy in an extruded Mg–Al–Ca–Mn alloy at cryogenic temperature. *Mater. Sci. Eng. A* **2024**, *890*, 145940. [CrossRef]

8. Kabir, A.S.H.; Sanjari, M.; Su, J.; Jung, I.-H.; Yue, S. Effect of strain-induced precipitation on dynamic recrystallization in Mg–Al–Sn alloys. *Mater. Sci. Eng. A* **2014**, *616*, 252–259. [CrossRef]
9. Sasaki, T.T.; Elsayed, F.R.; Nakata, T.; Ohkubo, T.; Kamado, S.; Hono, K. Strong and ductile heat-treatable Mg–Sn–Zn–Al wrought alloys. *Acta Mater.* **2015**, *99*, 176–186. [CrossRef]
10. Zhu, G.; Wang, L.; Zhou, H.; Wang, J.; Shen, Y.; Tu, P.; Zhu, H.; Liu, W.; Jin, P.; Zeng, X. Improving ductility of a Mg alloy via non-basal slip induced by Ca addition. *Int. J. Plast.* **2019**, *120*, 164–179. [CrossRef]
11. Pan, H.; Kang, R.; Li, J.; Xie, H.; Zeng, Z.; Huang, Q.; Yang, C.; Ren, Y.; Qin, G. Mechanistic investigation of a low-alloy Mg–Ca-based extrusion alloy with high strength–ductility synergy. *Acta Mater.* **2020**, *186*, 278–290. [CrossRef]
12. Zha, M.; Liang, J.-W.; Xing, H.; Xu, H.; Jiang, B.; Wang, C.; Jia, H.-L.; Wang, H.-Y. Spheroiding and refining of coarse CaMgSn phase in Mg–Al–Sn–Ca alloys for simultaneously improved strength and ductility via sub-rapid solidification and controlled rolling. *Mater. Sci. Eng. A* **2022**, *834*, 142598. [CrossRef]
13. Fan, G.D.; Zheng, M.Y.; Hu, X.S.; Xu, C.; Wu, K.; Golovin, I.S. Improved mechanical property and internal friction of pure Mg processed by ECAP. *Mater. Sci. Eng. A* **2012**, *556*, 588–594. [CrossRef]
14. Yoshimoto, S.; Miyahara, Y.; Horita, Z.; Kawamura, Y. Mechanical Properties and Microstructure of Mg-Zn-Y Alloys Processed by ECAE. *Mater. Sci. Forum* **2006**, *503–504*, 769–774. [CrossRef]
15. Shi, Y.; Zheng, J.; Ji, J.; Zhang, H.; Zhang, Z.; Wang, Q.; Xue, Y. The improvement of grain refinement, texture modification and mechanical properties of pure Mg prepared by cyclic expansion extrusion with an asymmetric extrusion cavity. *Mater. Res. Express* **2021**, *8*, 046530. [CrossRef]
16. Yang, Q.; Jiang, B.; Pan, H.; Song, B.; Jiang, Z.; Dai, J.; Wang, L.; Pan, F. Influence of different extrusion processes on mechanical properties of magnesium alloy. *J. Magnes. Alloys* **2014**, *2*, 220–224. [CrossRef]
17. Pan, F.; Wang, Q.; Jiang, B.; He, J.; Chai, Y.; Xu, J. An effective approach called the composite extrusion to improve the mechanical properties of AZ31 magnesium alloy sheets. *Mater. Sci. Eng. A* **2016**, *655*, 339–345. [CrossRef]
18. Wang, Q.; Jiang, B.; Tang, A.; Ma, S.; Jiang, Z.; Chai, Y.; Liu, B.; Pan, F. Ameliorating the mechanical properties of magnesium alloy: Role of texture. *Mater. Sci. Eng.: A* **2017**, *689*, 395–403. [CrossRef]
19. He, J.; Jiang, B.; Xie, H.; Jiang, Z.; Liu, B.; Pan, F. Improved tension-compression performance of Mg-Al-Zn alloy processed by co-extrusion. *Mater. Sci. Eng.: A* **2016**, *675*, 76–81. [CrossRef]
20. Jiang, Y.; Zhang, Z.; Wang, M.; Li, Y.; Cai, J.; Li, Z. Microstructure and mechanical properties of Mg-Al-Sn-Ca alloy extruded by asymmetric severe shear extrusion with different asymmetric coefficients. *J. Alloys Compd.* **2023**, *960*, 170884. [CrossRef]
21. Liu, L.; Wei, L.; Xiao, J.; Bai, S.; Jiang, B.; He, C.; Huang, G.; Zhang, D.; Pan, F. Improving mechanical properties of AZ31 alloy sheets via novel turned-bearing extrusion by introducing shear strain. *J. Mater. Res. Technol.* **2023**, *24*, 9915–9927. [CrossRef]
22. Yang, H.; Chai, Y.; Jiang, B.; He, C.; He, J.; Yang, Q.; Yuan, M. Enhanced mechanical properties of Mg-3Al-1Zn alloy sheets through slope extrusion. *Int. J. Miner. Metall Mater.* **2022**, *29*, 1343–1350. [CrossRef]
23. Zhao, C.; Li, Z.; Shi, J.; Chen, X.; Tu, T.; Luo, Z.; Cheng, R.; Atrens, A.; Pan, F. Strain hardening behavior of Mg–Y alloys after extrusion process. *J. Magnes. Alloys* **2019**, *7*, 672–680. [CrossRef]
24. Xu, J.; Yang, T.; Jiang, B.; Song, J.; He, J.; Wang, Q.; Chai, Y.; Huang, G.; Pan, F. Improved mechanical properties of Mg-3Al-1Zn alloy sheets by optimizing the extrusion die angles: Microstructural and texture evolution. *J. Alloys Compd.* **2018**, *762*, 719–729. [CrossRef]
25. Hansen, N. Hall–Petch relation and boundary strengthening. *Scr. Mater.* **2004**, *51*, 801–806. [CrossRef]
26. Yu, H.; Xin, Y.; Wang, M.; Liu, Q. Hall-Petch relationship in Mg alloys: A review. *J. Mater. Sci. Technol.* **2018**, *34*, 248–256. [CrossRef]
27. Liu, Y.; Cheng, W.; Zhang, Y.; Niu, X.; Wang, H.; Wang, L. Microstructure, tensile properties, and corrosion resistance of extruded Mg-1Bi-1Zn alloy: The influence of minor Ca addition. *J. Alloys Compd.* **2020**, *815*, 152414. [CrossRef]
28. Nie, J.F. Effects of precipitate shape and orientation on dispersion strengthening in magnesium alloys. *Scr. Mater.* **2003**, *48*, 1009–1015. [CrossRef]
29. Kang, D.H.; Kim, D.-W.; Kim, S.; Bae, G.T.; Kim, K.H.; Kim, N.J. Relationship between stretch formability and work-hardening capacity of twin-roll cast Mg alloys at room temperature. *Scr. Mater.* **2009**, *61*, 768–771. [CrossRef]